

Microwave magnetoplasma study of lattice and electronic properties of PbTe†

G. M. T. Foley* and D. N. Langenberg

Department of Physics and Laboratory for Research on the Structure of Matter, University of Pennsylvania,
Philadelphia, Pennsylvania 19104

(Received 13 September 1976)

The $q = 0$ transverse-optic-phonon frequency ω_{TO} has been determined in PbTe from microwave magnetoplasma experiments at frequencies near 70, 138, and 335 GHz, over the temperature range $4.2 \leq T \leq 80$ K. Both n -type and p -type bulk samples and p -type epitaxial thin films on BaF₂ substrates were studied. At the lowest temperatures, ω_{TO} is almost temperature independent and has the value $12.3 \pm 1.0 \text{ cm}^{-1}$. This implies, via the Lyddane-Sachs-Teller relation, a static lattice dielectric constant $\epsilon_s \cong 3000$, depending on the value assumed for the high-frequency dielectric constant ϵ_∞ . At temperatures above 30 K, ω_{TO} shows a temperature dependence which is consistent with Curie-law behavior of the static lattice dielectric constant, $\epsilon_s \propto (T - T_C)^{-1}$. Curie temperatures near both -150 and -80 K were found, but the favored experimental value is $T_C = -151 \pm 7$ K. Several band-edge electronic parameters were also determined: transverse-conduction-band-edge effective mass, $m_{1c}/m_0 = 0.0164 \pm 0.001$; transverse-valence-band-edge effective mass, $m_{1v}/m_0 = 0.021 \pm 0.001$; valence-band-edge mass anisotropy ratio, $K_0 = 13.4 \pm 2.0$. The critical importance of sample preparation and characterization procedures is discussed, together with possible reasons for the discrepancies among previously reported values of ϵ_s , which scatter over two orders of magnitude.

I. INTRODUCTION

The lead chalcogenides, PbS, PbSe, and PbTe, are narrow-gap semiconductors which have been extensively studied over the past several decades.¹ Much interest has centered on the lattice dielectric properties of these materials. They are polar, have large lattice dielectric constants, and, at least in the case of PbTe, exhibit a tendency toward a lattice structural instability associated with a soft phonon. PbTe has been particularly intensively studied; results of experiments related to the static lattice dielectric constant of this material are summarized in Table I. Notable is the scatter of the reported values of the static lat-

tice dielectric constant over nearly two orders of magnitude. This is certainly attributable in part to the strong temperature dependence of the dielectric constant, first demonstrated experimentally by Bate *et al.*,¹⁴ who found that the static lattice dielectric constant displays paraelectric Curie-law behavior. But major unexplained discrepancies remain. We report here extensive low-temperature magnetoplasma measurements on PbTe in a study of lattice and electronic properties intended to resolve these discrepancies. In particular, we have determined the static lattice dielectric constant ϵ_s and have confirmed that PbTe is indeed paraelectric.¹⁵ Further, we have employed a microwave conductivity technique to

TABLE I. Experimental values of the static lattice dielectric constant of PbTe.

Reference	ϵ_s	Experiment	Sample type	Temperature (K)
2	400	differential capacitance	p - n	77
2	430	differential capacitance	p - n	4.2
3	400	differential capacitance	p - n	77
3	500	tunneling analysis	p - n	77
4	≤ 200	surface impedance (24 GHz)	p	77-333
5	412	neutron scattering		300
6	1340	neutron scattering	p	4
7	397	ir absorption		4.2
8	3000	magnetoplasma (70 GHz)	p	4.2
9	10^4	magnetoplasma (70 GHz)	n	4.2
10	1300	magneto-optical	n	1.2
11	10^4	magnetoplasma (45 GHz)	n	4.2
11	3000	magnetoplasma	n	4.2
12	1410	magnetoplasma (50 GHz)	n	1.6
13	800	microwave conductivity (10 GHz)		300

establish a room-temperature value for ϵ_s (reported elsewhere¹³), permitting a comparison with extrapolated values from our low-temperature magnetoplasma measurements. Specifically, the magnetoplasma experiments reported here were carried out in reflection (i) at 70 GHz, repeating earlier measurements by Sawada *et al.*⁸ and by Perkowitz,⁹ and extending the measurements to the microwave bands centered at 138 and 335 GHz; (ii) on both *p*- and *n*-type bulk single crystals and *p*-type epitaxial thin films; (iii) over a range of carrier concentrations; (iv) over a range of temperatures.

Observations of cyclotron resonance in the course of the magnetoplasma experiments have yielded transverse cyclotron effective masses and (for *p*-type samples) a mass anisotropy ratio. A careful re-evaluation of nonlocal effects has been made. The significance of these measurements in the context of a new parametrization of a multi-band model of the PbTe conduction and valence bands is discussed in the following paper.¹⁶

Particular attention has been paid throughout the work to materials preparation and sample characterization. Some significant observations in this regard are reported, and attention is drawn to a number of problems which represent possible sources of the aforementioned discrepancies among reported parameter values.

II. THEORY

A. Dielectric function

For the analysis of our experimental data, we require the frequency- and wave-vector-dependent dielectric function $\epsilon(q, \omega)$. Spatial dispersion (wave-vector dependence) is important in the analysis of effective masses from the cyclotron resonance data and will be discussed in that context. Otherwise, it suffices in the present case to consider $\epsilon(0, \omega)$, the dielectric function in the long-wavelength or local limit.

Varga¹⁷ has shown that the contributions of the "bare" lattice and the free carriers to the total dielectric function can be considered separately and then summed. We consider first the lattice contribution. Lead telluride crystallizes in the cubic rocksalt structure with two atoms per unit cell. The appropriate frequency-dependent local lattice dielectric constant $\epsilon_L(\omega)$ is therefore¹⁸

$$\epsilon_L(\omega) = \epsilon_\infty + \epsilon_\infty(\omega_{LO}^2 - \omega_{TO}^2)/(\omega_{TO}^2 - \omega^2 + i\omega\Gamma). \quad (1)$$

The high-frequency dielectric constant ϵ_∞ represents contributions from interband transitions. In the present experiments, ω was sufficiently small that ϵ_∞ may be regarded as frequency independent. ω_{LO} and ω_{TO} are the longitudinal- (LO) and trans-

verse- (TO) optical normal-mode lattice frequencies. Γ is a phenomenological lattice damping factor. The static lattice dielectric constant ϵ_s is defined as the zero-frequency limit $\epsilon_L(0)$. In the limit of zero wave vector, the Lyddane-Sachs-Teller relation¹⁹ provides a useful connection between ϵ_s , ϵ_∞ , and the normal-mode frequencies:

$$\omega_{LO}^2/\omega_{TO}^2 = \epsilon_s/\epsilon_\infty. \quad (2)$$

We now consider the free-carrier contribution to the total dielectric function. The Fermi surface for PbTe, both *n*- and *p*-type, consists of eight half-ellipsoids with principal axes along the $\langle 111 \rangle$ directions in the Brillouin zone.¹ The magnetoplasma experiments discussed here were carried out exclusively in the Faraday configuration in which the wave vector of the incident radiation was either parallel or antiparallel to an applied magnetic field \vec{H} . Only the high symmetry orientations $\vec{H} \parallel \langle 100 \rangle$ and $\vec{H} \parallel \langle 111 \rangle$ were investigated. For these cases, the electronic response of the medium may be characterized by scalar dielectric functions ϵ_{el}^+ and ϵ_{el}^- corresponding to right- and left-circularly polarized electromagnetic normal modes. The two modes are often called the cyclotron-resonance-active (CRA) and cyclotron-resonance-inactive (CRI) modes. The active mode is that for which the sense of rotation of the electromagnetic field is the same as that of the orbital motion of the carriers about the magnetic field. The local dielectric functions appropriate to the band structure of PbTe, assuming a parabolic ellipsoidal model for the Fermi surface, are²⁰ for $\vec{H} \parallel \langle 100 \rangle$:

$$\epsilon_{el}^\pm = 1 - \frac{\omega_p^2}{\omega} \frac{(\omega + i\nu) \mp \omega_3}{(\omega + i\nu)^2 - \omega_c^2}, \quad (3)$$

where

$$\omega_p^2 = \frac{4\pi ne^2}{m_1} \left(\frac{2K+1}{3K} \right); \quad \omega_3 = \frac{m_0}{m_1} \left(\frac{K+2}{2K+1} \right) \omega_{c0}; \quad (4)$$

$$\omega_c^2 = \frac{m_0^2}{3m_1^2} \left(\frac{K+2}{K} \right) \omega_{c0}^2; \quad \omega_{c0} = \frac{eH}{m_0 c},$$

where

$$e = \pm |e|, \quad K = m_3/m_1.$$

m_3 and m_1 are the longitudinal and transverse carrier effective masses, respectively, and m_0 is the free-electron mass. For $\vec{H} \parallel \langle 111 \rangle$:

$$\epsilon_{el}^\pm = 1 - \frac{\omega_{p0}^2}{4\omega} \left(\frac{m_0}{m_1[(\omega + i\nu) \pm \omega_{c1}]} - \frac{m_0}{3m_1K} \frac{(5K+4)(\omega + i\nu) \mp (K+8)\omega_{c1}}{\omega_{c2}^2 - (\omega + i\nu)^2} \right), \quad (5)$$

where

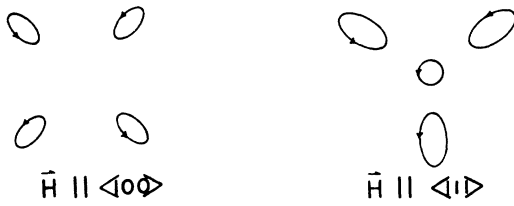


FIG. 1. Free-carrier orbits in a magnetic field for PbTe.

$$\begin{aligned} \omega_{p0}^2 &= 4\pi ne^2/m_0; \quad \omega_{c1} = (m_0/m_1)\omega_{c0}; \\ \omega_{c2} &= \frac{m_0}{m_1} \left(\frac{K+8}{9K} \right)^{1/2} \omega_{c0}. \end{aligned} \quad (6)$$

The carrier cyclotron orbits in momentum space in the plane perpendicular to \vec{H} are shown in Fig. 1 for both field orientations. The elliptical orbits correspond to a cyclotron frequency which is a function of both m_1 and K . For $\vec{H} \parallel \langle 111 \rangle$ there is a circular orbit with a cyclotron frequency depending only on m_1 . The dielectric functions [Eqs. (3) and (5)] indicate that a cyclotron resonance corresponding to the elliptical orbits occurs in both ϵ_{\parallel}^+ and ϵ_{\parallel}^- . This results from the fact that if the elliptical orbits are resolved into circular components, a circular component with rotation sense opposite to that of the elliptical orbit remains. A circularly polarized electromagnetic field of either polarization can therefore couple resonantly to the cyclotron motion.

The total dielectric function of the system is simply¹⁷

$$\epsilon^{\pm} = \epsilon_L + \epsilon_{cl}^{\pm} - 1. \quad (7)$$

B. Resonances and dielectric anomalies

We are interested in two types of singularities in the dielectric function [Eq. (7)]—the poles and the zeros. The poles correspond to resonances, i.e., the cyclotron resonances and the resonance associated with the TO phonon mode. The zeros are associated with mixed phonon-plasmon normal modes resulting from the strong coupling between the longitudinal optic phonon and the free carrier plasma. For purposes of the present discussion we define a dielectric anomaly as a zero in the real part of $\epsilon^{\pm}(\omega)$.

The amplitude reflection coefficient at the interface of a vacuum and a semi-infinite medium with dielectric constant ϵ is given by

$$R = (Z - 1)/(Z + 1), \quad (8)$$

where $Z \propto \epsilon^{-1/2}$. Zeros in $\text{Re}\epsilon$ correspond very closely to minima in reflection at such an interface. Experimentally, therefore, we may locate

dielectric anomalies by observation of minima in reflectivity.

Figure 2 shows the loci of the singularities in the total dielectric function in the (ω, H) plane for $\vec{H} \parallel \langle 100 \rangle$. Figure 3 shows the corresponding loci for $\vec{H} \parallel \langle 111 \rangle$. (For clarity, parameter values different from those appropriate to PbTe have been used in generating Figs. 2 and 3.) Loci lying to the left of the ω axis correspond to the cyclotron-resonance-inactive mode (ϵ^- for electrons), while those to the right correspond to the cyclotron-resonance-active mode (ϵ^+ for electrons). Dashed lines represent the resonances (poles), solid lines the dielectric anomalies (zeros). In the unshaded regions, $\text{Re}\epsilon$ is positive and propagating (helicon) modes exist. In the shaded regions, $\text{Re}\epsilon$ is negative and no propagating modes exist. We have neglected damping ($\nu = \Gamma = 0$) in Figs. 2 and 3. The effects of damping are especially important in the vicinity of the resonances (dashed lines).

The principal focus of our attention in the present experiments has been one particular dielectric anomaly, that which occurs in the CRI mode and is lowest in frequency in the (ω, H) plane. In PbTe, this anomaly is accessible in moderate magnetic fields at microwave frequencies and has the virtue that its magnetic field position is very sensitive to the value of the TO phonon frequency. The manner in which this anomaly arises is indicated in

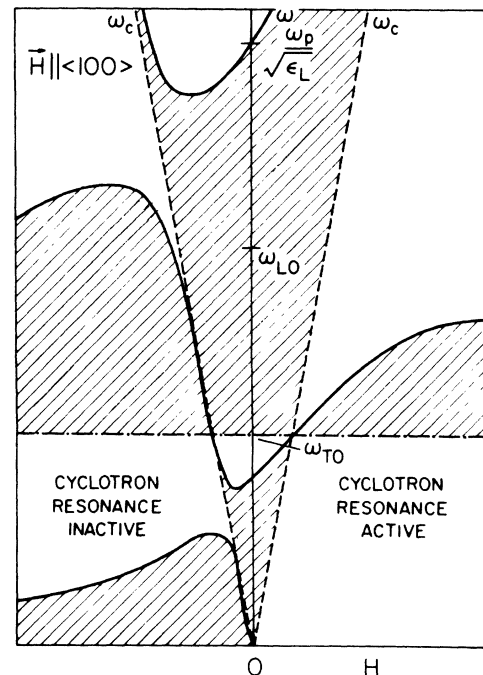


FIG. 2. Loci of dielectric function singularities in the (ω, H) plane for $\vec{H} \parallel \langle 100 \rangle$.

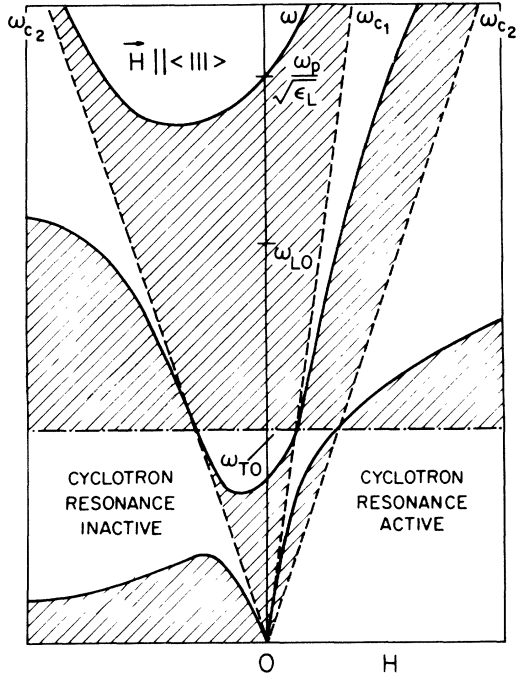


FIG. 3. Loci of dielectric function singularities in the (ω, H) plane for $\vec{H} \parallel \langle 111 \rangle$.

Fig. 4, which shows the free-carrier contribution to the CRI mode dielectric constant as a function of cyclotron frequency (magnetic field) for the $\vec{H} \parallel \langle 100 \rangle$ configuration. (The picture is similar for the $\vec{H} \parallel \langle 111 \rangle$ case.) ϵ_{el} for the CRI mode has a pole at $\omega_c = \omega$ corresponding to the elliptical orbit cyclotron resonance. For $\omega_c > \omega\omega_c/\omega_3$, ϵ_{el} is negative. Now the principal microwave frequencies used in our experiments correspond to wave numbers about 2.3 and 4.6 cm^{-1} and are almost certainly less than ω_{TO} , however speculative its value. Hence ϵ_L is clearly positive, and can be cancelled by the negative ϵ_{el} [provided $|\epsilon_{el}(\text{min})| > |\epsilon_L|$] at the two values of ω_c/ω marked A and B in Fig. 4. The anomaly at A is close to the cyclotron resonance at $\omega_c/\omega = 1$ and the two will tend to be intermixed and the anomaly not clearly distinguishable. The anomaly at B, however, is both well removed from the cyclotron resonance and highly sensitive to ω_{TO} , the latter because $\partial\epsilon_{el}/\partial H$ is relatively small near B. This anomaly has two important distinguishing features: (a) It moves to higher fields with decreasing frequency, in contrast to the cyclotron resonance and the neighboring anomalies. (b) If ϵ_s decreases and ω_{TO} increases with increasing temperature, the anomaly will also move to higher fields.

We note in passing that experimental signals associated with a dielectric anomaly may be ex-

pected to have a characteristic shape which can serve as a useful check on identification of the anomaly. Neglecting damping for the moment, as one passes through the anomaly from negative ϵ to positive ϵ , the reflectivity drops precipitously from 1 to 0, then increases more slowly toward a value less than one. (The latter may be nearly one if the positive ϵ becomes large.) In our experiments, the frequency was held constant and ϵ is varied by varying the magnetic field. Since field modulation was used, the quantity of interest is dR/dH . The expected form of dR/dH at a dielectric anomaly is sketched in Fig. 5, including damping, for $\partial\epsilon/\partial H$ both positive and negative at the anomaly field.

C. Helicon phase oscillations

The amplitude reflection coefficient R for a dielectric slab of thickness d at normal incidence is given by

$$R = \alpha_3 \alpha_2 (1 - e^{2iqd}) / (\alpha_2^2 - \alpha_3^2 e^{2iqd}), \quad (9)$$

where q is the wave vector of the appropriate propagating normal mode in the dielectric, $\alpha_2 = Z_0^{-1} + Z^{-1}$, and $\alpha_3 = Z_0^{-1} - Z^{-1}$, where Z_0 and Z are, respectively, the free-space and dielectric complex impedances defined through $Z = \mu\omega/cq$. Neglecting multiple reflections, the phase of R is given approximately by $\varphi \cong 2q_1 d$, where $q_1 = \text{Re}q$. If q_1 varies, R will show periodic oscillations with period given by $2q_1 d = 2\pi n_0$, where n_0 is the number of 2π phase shifts in the sample thickness. Now

$$\begin{aligned} q_1 &= \frac{\omega}{c} \text{Re}\epsilon^{1/2} \\ &= \frac{\omega}{c} \left\{ \epsilon_L + \frac{\omega_p^2}{\omega\omega_{c0}} \left[1 + \frac{K(K+2)}{2K+1} \left(\frac{\omega}{\omega_{c0}} \right) + \dots \right] \right\}^{1/2}, \end{aligned} \quad (10)$$

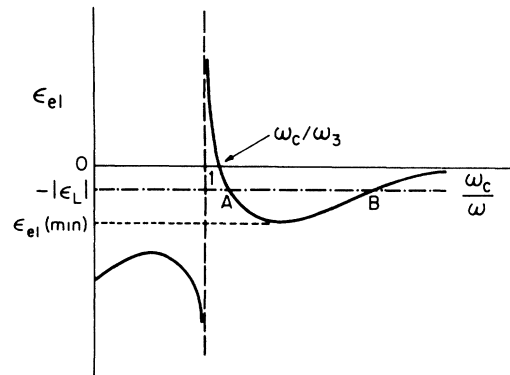


FIG. 4. Free-carrier dielectric constant versus magnetic field for the CRI mode in the $\vec{H} \parallel \langle 100 \rangle$ configuration.

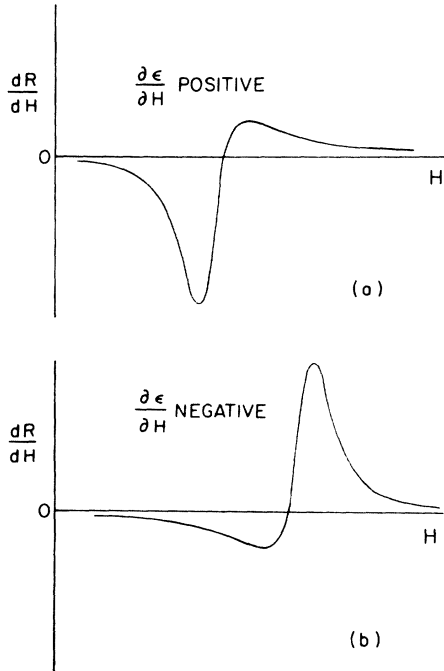


FIG. 5. Characteristic line shapes of reflectivity derivative in the region of a dielectric anomaly.

where the second equation contains an expansion of ϵ_{el} for $\vec{H} \parallel \langle 100 \rangle$ [Eq. (3)]. In the so-called helicon limit where we may neglect ϵ_L and retain only the first term in the expansion, the periodicity condition becomes

$$(\omega_p^2 \omega d^2 / \omega_c c^2)^{1/2} \approx \pi n_0. \quad (11)$$

We expect, therefore, that in the helicon propagation regime the reflectivity of a slab sample will display oscillations periodic in $H^{-1/2}$.

D. Effective masses

We are interested in deriving band edge effective masses¹⁶ from observed cyclotron resonances. In doing so, two effects must be corrected for, the Doppler shift of the resonance due to nonlocal effects, and the fact that the observed resonance is due to electrons or holes at the Fermi surface, not the band edge. In the present experiments the latter correction was based on the band-structure model discussed in detail in the following paper.¹⁶ Correction for nonlocal effects was made using the following theory: For electrons or holes with spherical isoenergetic surfaces, in the limit of small damping and weak nonlocality, the cyclotron resonance condition becomes²¹

$$\omega_c = (1 + \rho^{1/3}) \omega, \quad (12)$$

where

$$\rho = \omega_p^2 v_F^2 / 5 \omega^2 c^2 \quad (13)$$

measures the degree of nonlocality. For an ellipsoidal parabolic energy-band model appropriate to PbTe for the carrier concentrations of interest here, Perkowitz²² found that the nonlocality parameter ρ may be defined by

$$\rho = \omega_p^2 v_{F\text{eff}}^2 / \omega^2 c^2, \quad (14)$$

where

$$v_{F\text{eff}}^2 = \alpha v_F^2 = \frac{1}{N} \int_{\text{FS}} (\hat{n} \cdot \vec{v})^2 d^3v, \quad (15)$$

$$N = \int_{\text{FS}} d^3v. \quad (16)$$

Here the indicated integrals are over the Fermi surface and \hat{n} is a unit vector along \vec{H} . The general expression for the parameter α , with \vec{H} at an angle θ with respect to the principal axis of a spheroidal Fermi surface, is

$$\alpha = (K \sin^2 \theta + \cos^2 \theta) / 5K^{2/3}. \quad (17)$$

For the cases of interest here: $\vec{H} \parallel \langle 100 \rangle$,

$$\alpha = (2K + 1) / 15K^{2/3}; \quad (18)$$

and for $\vec{H} \parallel \langle 111 \rangle$, circular orbit:

$$\alpha = (5K^{2/3})^{-1}; \quad (19)$$

and elliptical orbits:

$$\alpha = (8K + 1) / 45K^{2/3}. \quad (20)$$

Even at low ($\sim 2 \times 10^{17} \text{ cm}^{-3}$) carrier concentrations the nonlocal correction to the effective masses is important in PbTe.

III. SAMPLE PREPARATION AND CHARACTERIZATION

The matter of sample preparation and characterization has proven to be a highly important aspect of this research. PbTe has a number of unusual properties which make difficult the preparation of quasiperfect crystals. It is highly susceptible to mechanical damage and to chemical contamination. Great care is therefore necessary at every stage of sample preparation. In the course of our work it has become painfully evident that several types of diagnostic measurements which are commonly used to characterize sample quality and parameters can be quite misleading. Epitaxial thin films, which require no further preparation after growth, and which at every stage of that growth are under carefully controlled conditions, are often to be preferred over bulk crystals, which require considerable handling in preparation for microwave measurements.

We have made measurements both on bulk single crystals and epitaxial thin films grown on barium

TABLE II. Sample identification.

Type	Designation	Source
Bulk <i>p</i> -type	1	A. J. Strauss, Lincoln Labs.
Bulk <i>n</i> -type	2, 3, 4, 5, 6, 7	K. Sawada, M.I.T.
Thin-film <i>p</i> -type	8, 9	H. Holloway, Ford Res. Labs.

fluoride. (Some room-temperature microwave conductivity measurements have also been made using fine single-crystal whiskers.¹³) Our samples and their sources are listed in Table II. The thin-film samples were annealed and characterized by Holloway and used by us as received without further treatment or characterization. These films were oriented with $\langle 111 \rangle$ axes normal to the film plane. Our experiments on these samples were therefore performed with $\vec{H} \parallel \langle 111 \rangle$ instead of $\vec{H} \parallel \langle 100 \rangle$, the orientation used for all the other (bulk) samples. This made analysis of the data somewhat more difficult than it would have been for films grown on rocksalt substrates with $\langle 100 \rangle$ orientation. However, films on barium fluoride are superior in carrier mobility, and the barium fluoride substrate also provides a better thermal expansion match to PbTe, minimizing (but not eliminating) strain on cooling.

Samples of high carrier mobility are essential in experiments of the present type. Thus, as-grown samples, which typically have low mobilities even at helium temperatures, must be annealed. The Holloway and Strauss samples were received already annealed. The bulk *n*-type samples were annealed by us using the isothermal technique.²³ Prior to annealing, small pieces of the as-grown crystal were cut with approximately $\{100\}$ faces, using the lowest spark energy on a Servomet spark-cutter ($5 \mu\text{J}$). The use of low spark energies in cutting crystals is absolutely essential. Damage from spark cutting can extend hundreds of microns into a single crystal if this precaution is not taken. Experience showed that simple washing of samples in acetone after spark cutting was inadequate to remove from the surface the debris collected in cutting. (Ultrasonic cleaning should never be considered.) The Coates²⁴ chemical etch was found to produce nice clean surfaces. After spark cutting, all samples were annealed with lead-rich ingots of PbTe to produce *n*-type samples. By this means, samples of high mobility and carrier concentrations in the desired 10^{17} cm^{-3} range were obtained.

After annealing, the samples were first oriented by the conventional Laue back-scattering technique, and then spark-planed on both sides on the lowest spark energy scale. This method per-

mitted orientation to within $\frac{1}{2}^\circ$ of the $\langle 100 \rangle$ axis. Disks 6 mm in diameter and approximately $\frac{1}{2}$ mm thick were finally cut from the planed slices for microwave measurements.

Several polishing procedures were tried during the course of this work. Ultimately it became apparent that the procedure used critically affected the quality of the results. Mygind¹¹ has noted in his preparation of samples for microwave transmission experiments that mechanical polishing methods appeared to be superior to electrolytic polishes. While it is true that a high degree of flatness and parallelism of the sample is not easily achieved using electrolytic methods, it appears that even the finest mechanical polish, though producing a visibly mirrorlike surface, may induce damage in the sample extending to a significant depth (many tens of microns). This has been noted in the literature in measurements of sample damage using etch pit count techniques rather than low-energy x-ray diffraction.²⁵ The necessity for using an electrolytic polish to obtain reproducible results in infrared reflectivity measurements has also been noted by Dixon and Riedl,²⁶ and by Dionne and Woolley.²⁷

The problem of sample surface damage has been a major one in our work. Its importance early became apparent when we found that a clearly observable dielectric anomaly disappeared completely after the sample was mechanically polished with $6\text{-}\mu\text{m}$ diamond paste and then electropolished for 3 min using the Norr method,²⁸ at a nominal material-removal rate of $7 \mu\text{m}/\text{min}$. We then moved to a procedure similar to that described by Dionne and Woolley,²⁹ involving two 10-min electropolishes before and after a very light mechanical polish using 1- and $3\text{-}\mu\text{m}$ alumina powder, intended to maintain flatness of the sample surfaces. Samples prepared in this manner *appeared* to give excellent results. Figure 6(a) shows an experimental trace for a sample so prepared. The large signal at about 40 kG is identified as the dielectric anomaly of interest. Its size and shape, as well as those of the cyclotron resonance signal at low fields, suggest a relatively undamaged and homogeneous sample. However, further electropolishing of this sample produced the dramatic shift of the dielectric anomaly signal shown in Fig. 6(b).

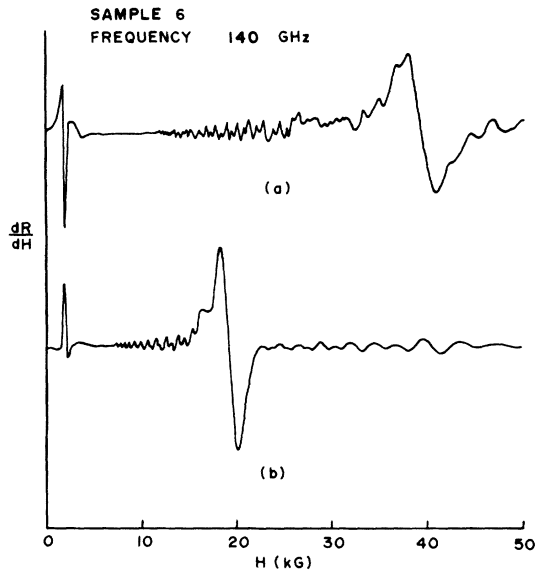


FIG. 6. Reflectivity data (a) after mechanical polish and electropolish and (b) after further electropolish.

The shift corresponds to an apparent change of a factor of 2 in carrier concentration! The change in the width of the anomaly signal is less dramatic, although it did narrow somewhat.

Since it is known that lattice vacancies in PbTe contribute free carriers,³⁰ it is reasonable to suppose that vacancies and dislocations produced by mechanical polishing will modify the carrier concentration in the damaged region. This can have a substantial effect on carrier-concentration-sensitive phenomena like the dielectric anomaly. (Note that the cyclotron resonance, which should not be very sensitive to carrier concentration, shows no significant shift in Fig. 6.) However, since mechanical damage is concentrated in some region near the sample surface, the damage-induced carrier density should be rather inhomogeneous. It is difficult to understand, therefore, how damage sufficient to produce the change in carrier concentration implied by the data of Fig. 6 would not also be accompanied by sufficient inhomogeneity of carrier density to produce a large broadening of the dielectric anomaly signal. The answer may be that the penetration depth of the microwave radiation in the vicinity of the dielectric anomaly remains sufficiently small compared with the depth of the mechanical damage region so that the radiation effectively probes a surface layer where the carrier density is relatively homogeneous but quite different from the density in the interior of the sample.

Whatever the mechanism responsible for the effect apparent in Fig. 6, it is abundantly clear that

wherever PbTe has been mechanically polished and a carrier-concentration-sensitive experiment done which probes the sample surface, any conclusions which depend on the assumption that the surface and bulk carrier concentrations are homogeneous and equal are highly suspect, regardless of the apparent "quality" of the data. Consequently, in the experiments reported here all mechanical polishing was eliminated and samples prepared using the Norr electropolish technique exclusively. After spark planing, each sample was repolished and rerun in successive stages until the experimental traces became completely reproducible or until the sample was deemed unsatisfactory and discarded. Acceptable samples typically required the removal of at least 100 μm of material from the surfaces.

A word of caution with respect to contamination of the sample is also necessary. Lead telluride has among its peculiar properties a very high diffusion constant and is therefore highly prone to surface contamination. Many possible contaminants form donors or acceptors in the material.³¹ We found, for example, that it is essential to keep silver paint on the sample surface to a minimum while mounting for spark cutting or electropolishing. In one instance, we observed that silver paint contamination caused the complete disappearance of a previously observed dielectric anomaly signal.

We made conventional Hall measurements on our *n*-type samples to determine bulk carrier concentrations and carrier mobilities. The Hall samples were cut from the source crystal adjacent to the portion used for microwave measurements and had dimensions approximately $1 \times 2 \times 8$ mm. Measurements were made over a range of temperatures between 4.2 K and room temperature. Data for three temperatures are shown in Table III. The indicated carrier concentrations were calculated from the standard high-field-limit expression, $n = (eR_\infty)^{-1}$, where R_∞ is the Hall constant measured at about 1.5 kG. This is strictly valid only if the criterion $\mu H > 10^8$ (μ is the mobility in $\text{cm}^2/\text{V sec}$, H in G) is satisfied, so that only the 4.2 K values are truly appropriate to this limit.

The mobilities were calculated from $\mu(T) = R_\infty(4.2)\sigma(T)$, where $\sigma(T)$ is the measured conductivity at temperature T . This is the same procedure adopted by Allgaier and Houston,³² and is justified on the basis that no freeze-out of carriers is expected, theoretically or on the basis of experimental data. The mobility of our samples was typically 10^3 $\text{cm}^2/\text{V sec}$ at room temperature, rising to about 10^6 $\text{cm}^2/\text{V sec}$ at 4.2 K.

Subsequent to the three-temperature measurements of Table III, more detailed measurements

TABLE III. Carrier concentrations and Hall mobilities for (bulk) *n*-type samples.

Sample	$n_{4.2}$ (cm^{-3})	n_{77} (cm^{-3})	n_{300} (cm^{-3})	$\mu_{4.2}$ ($\text{cm}^2/\text{V sec}$)	μ_{77} ($\text{cm}^2/\text{V sec}$)	μ_{300} ($\text{cm}^2/\text{V sec}$)
2	1.14×10^{17}	1.32×10^{17}	1.92×10^{17}	1.06×10^6	2.58×10^4	1.27×10^3
3	2.77	2.86	3.49	1.65	2.99	1.36
4	2.56	3.33	4.94	1.66	3.04	1.81
5	0.81	1.05	2.35	0.23	1.24	1.71
6	2.11	2.59	3.70	1.32	2.46	1.12
7	1.36	1.71	2.05	1.03	2.72	1.35

of the temperature dependence of the Hall mobility between 4.2 and 77 K were made. These measurements were made on the same Hall samples previously used. In particular, the sample leads remained intact from the earlier experiments, and therefore the lead geometry in the two sets of measurements was identical. The time lapse since the earlier measurements was approximately six weeks. The new measurements indicated that the carrier concentrations had all decreased by amounts in the range (10 to 20)%. The new measured carrier concentrations are shown as a function of temperature in Fig. 7. Again n has been computed uncritically from $n = (eR_\infty)^{-1}$. This substantial downward drift in carrier concentration (with time) for *n*-type lead telluride has been observed by others.^{33,34} It has been ascribed to precipitation of excess lead during room-temperature annealing.³⁴ The effect was observed in rather dramatic form and reported by Walpole in his unpublished dissertation,³³ but unfortunately it went unmentioned in the publication based on that work.³⁵ As a result, it represents a pitfall probably unrecognized by the majority of workers in the field, as evidenced by the lack of comment on the effect in recent literature. Since many of the experiments aimed at determining the TO phonon frequency in PbTe depend critically upon the value of the carrier density, it is important that measurements of carrier concentration be made coin-

cidently with experiments to determine ω_{TO} , in *n*-type samples, or that the relatively rapid drift of carrier concentration with time be recognized and accounted for. A similar effect is not expected or observed in *p*-type samples, where diffusion rates are smaller.

The data of Fig. 7 indicate that R_∞ decreases above about 60 K. It is significant that the criterion $\mu H > 10^8$ indicates a departure from the high-field limit at approximately this temperature. Below 60 K the curves show an approximately constant R_∞ down to 4.2 K. The apparent decrease in R_∞ between 60 and 300 K is typical of *n*-type samples in this concentration range.³⁶

If we assume that the lattice scattering rate τ_L^{-1} and the defect scattering rate τ_0^{-1} are independent, so that the total scattering rate is simply $\tau^{-1} = \tau_L^{-1} + \tau_0^{-1}$, and that at helium temperatures scattering is entirely by defects and temperature independent, then we may subtract the defect contribution from the total scattering rate and so deduce the lattice contribution. Plotting the corresponding mobility $\mu_L(T)$ vs T^{-1} , we find that, except for sample 5, which has a poor 4.2 K mobility, the temperature dependence of μ_L is given approximately by $\mu_L \propto T^{-2.3}$ for all samples between room temperature and 77 K. This is in good agreement with other published temperature dependences.^{32,37}

Characteristics of the *p*-type Strauss and Holloway samples are shown in Table IV. It should be noted that in making calculations from our data for the Holloway thin films we have made an extrapo-

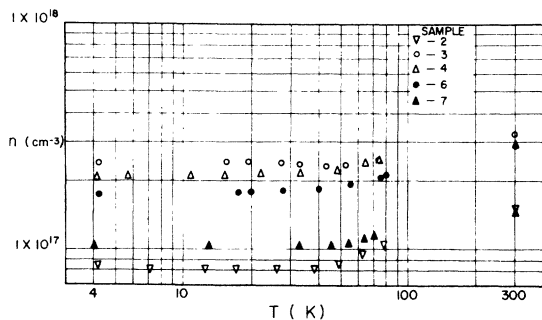


FIG. 7. Carrier concentration vs temperature for *n*-type PbTe.

TABLE IV. Carrier concentrations and Hall mobilities for *p*-type samples.

Sample	n (cm^{-3})	μ ($\text{cm}^2/\text{V sec}$)
1 ^a	5.4×10^{17}	...
8 ^b	5.4×10^{16}	1.8×10^4
9 ^b	5.4×10^{16}	1.8×10^4

^aThermoelectric measurement.

^b77 K values.

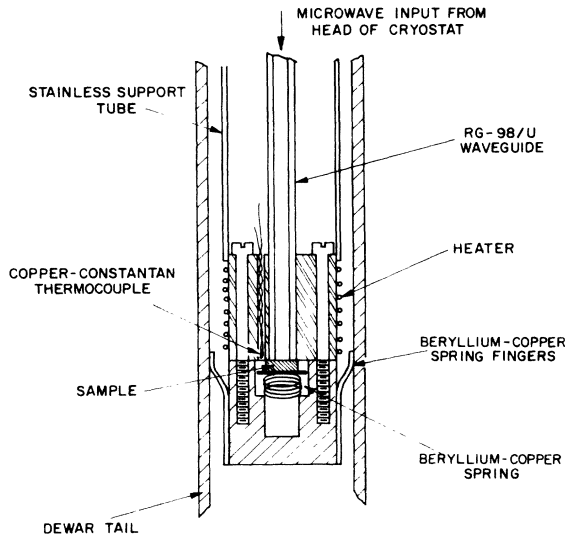


FIG. 8. Reflectivity microwave head.

lation of the carrier concentration measured at 77 to 4.2 K using a temperature dependence typical for such samples. The result is $n(4.2) = 4.6 \times 10^{16} \text{ cm}^{-3}$. This correction has, in fact, minimal effect on the final results.

IV. EXPERIMENTAL DETAILS

Measurements were made in reflection in the Faraday configuration using a conventional microwave bridge system at frequencies near 70, 138, and 335 GHz. Use of the reflection mode permitted the use of a room-temperature wire bolometer detector usable in all three frequency bands. It also permitted the use of a nominally linearly polarized microwave input signal, since the sample reflectivity change at a dielectric anomaly is quite large even without good circular polarization of the input signal. In contrast, in transmission, attenuation of the CRI mode in the sample is large and the relative change in transmission at a dielectric anomaly for linear input polarization is typically extremely small.

The total signal reaching the detector consists of a coherent superposition of the signal reflected from the sample and an adjustable reference signal from the microwave source. The use of the reference signal enhances the sensitivity of the system and also makes it sensitive to the *phase* of the sample reflectivity.

The essential features of the sample holder are shown in Fig. 8. RG-98/U (70-GHz) waveguide was used in the sample holder in all three frequency bands.

The sample was mounted on a flange flush against the end of the waveguide and constrained by

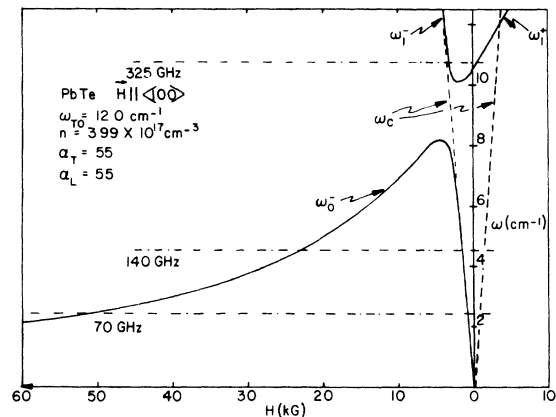
a small beryllium copper spring. At 70 GHz, only one component of the elliptically polarized wave reflected from the sample can propagate back up the guide for detection. This made detailed line-shape analysis of the data difficult, but identification and location of the important features of the microwave spectrum were generally still straightforward. At 2-mm wavelengths, 2-mm bridge components were matched to the 4-mm sample holder waveguide through a tapered transition. No 1-mm components were available so the 1-mm experiments were done using the bare minimum of 2-mm components. Temperature control of the sample over the range 4.2 to 85 K was achieved using a heater coil wound noninductively around the sample mounting block and a copper-Constantan thermocouple located in the block close to the sample.

A magnetic field parallel to the sample-holder waveguide axis was provided by a 60 kG superconducting magnet. A parallel modulation field at about 37 Hz with a maximum peak-to-peak amplitude of 600 G was provided by a superconducting coil. Phase-sensitive detection at the modulation frequency was used.

To ensure accuracy in measurement of microwave frequencies, the wavemeters used were calibrated using microwave-induced steps in the I - V characteristic of a niobium-niobium point contact Josephson device.

V. EXPERIMENTAL RESULTS, ANALYSIS, AND DISCUSSION

In considering our experimental results, it is useful to bear in mind dielectric anomaly plots like those given in Figs. 2 and 3. We consider first our bulk-sample results, all of which correspond to $\vec{H} \parallel \langle 100 \rangle$. Figure 9 is a dielectric anomaly

FIG. 9. Dielectric anomaly loci for $\vec{H} \parallel \langle 100 \rangle$ and parameters typical of the n -type bulk samples.

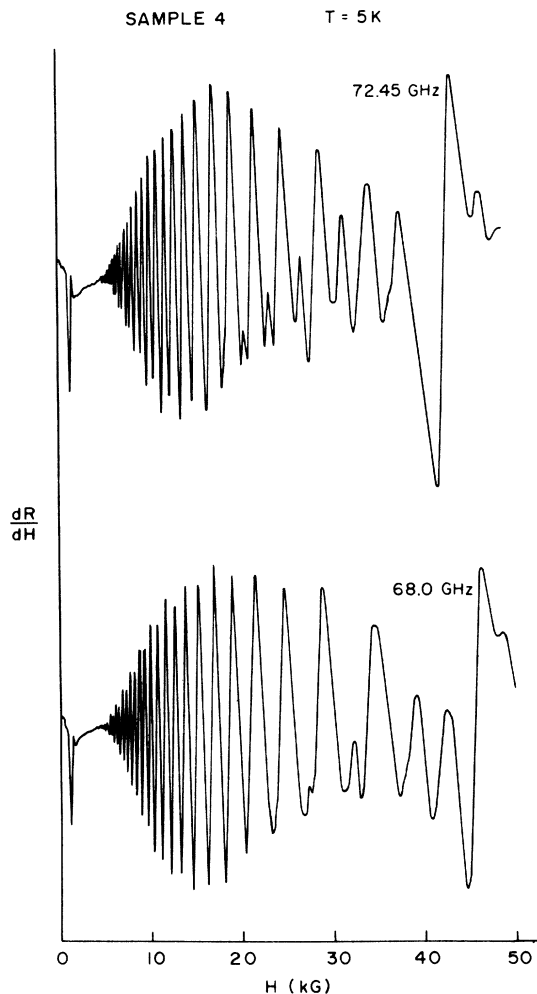


FIG. 10. Reflectivity data for sample 4 (bulk n -type) in the 4-mm band with $\vec{H} \parallel \langle 100 \rangle$.

ally plot for this case, corresponding to the lower portion of Fig. 2, but calculated for realistic parameters appropriate to the present experiments. For convenience, we shall henceforth label the anomaly branches in a manner appropriate to n -type samples, regardless of the carrier type under discussion. Thus ω_0^- denotes the anomaly branch lying lowest in frequency on the CRI side, ω_1^+ is the next highest branch on the CRA side, etc.

A. Bulk samples

1. Qualitative features of data

Typical experimental traces (here for sample 4) are shown for the 4-mm band in Fig. 10 and for the 2-mm band in Fig. 11. Remembering that the incident microwave radiation is nominally linearly polarized, so that both the CRA and CRI responses

appear together, we can identify the following principal features: at very low fields there is a sharp signal at a field which *increases* with increase in frequency. This is a mixture of the cyclotron resonance and the nearby low-field part of the ω_0^- anomaly. At somewhat higher fields a series of oscillations begins. These are helicon phase oscillations. As the field increases above the cyclotron resonance field, the attenuation of the propagating helicon mode in the CRA polarization component decreases rapidly and the finite thickness of the sample becomes important. The phase of the sample reflectivity becomes strongly field dependent, as discussed in Sec. II C, resulting in oscillations in the phase-dependent microwave bridge signal.

We attribute the double-frequency oscillation, which appears above 20 kG, to multiple reflections within the sample. If $\text{Im}qd$ in Eq. (9) becomes small, e.g., for thin samples at moderate to high fields, then the second term in the denominator of this equation can become non-negligible. This will give rise to a double-frequency oscillation.

At a field near 40 kG at 4 mm and near 20 kG at 2 mm another sharp signal appears. This is the dielectric anomaly signal. It has the characteristic feature that the anomaly field *decreases* with increase in frequency, as evidenced both by the large shift between 4 and 2 mm and the smaller shift apparent in Fig. 10 for two frequencies within the 4-mm band. Above the dielectric anomaly field, both the CRA and CRI modes can propagate, and the character of the phase oscillations changes.

The temperature dependence of the dielectric anomaly signal is shown in Fig. 12. As temperature increases, it broadens and moves to higher field, but remains observable up to 70–80 K.

We were unable to obtain any reliable data from our bulk samples in the 1-mm band. Fortunately, as we shall see in discussing the thin-film data, data from this frequency region, while interesting, are not of great importance in determining ω_{T0} .

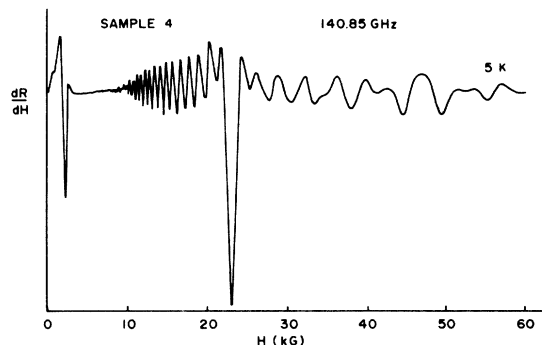


FIG. 11. Reflectivity data for sample 4 (bulk n -type) in the 2-mm band with $\vec{H} \parallel \langle 100 \rangle$.

2. Determination of ω_{TO}

The condition for the dielectric anomaly given by solution of the equation $\text{Re}\epsilon = 0$ may be written for the $\vec{H} \parallel (100)$ orientation in the form

$$\epsilon_L(\omega) = (\omega_p^2/\omega)f(H_a), \quad (21)$$

where

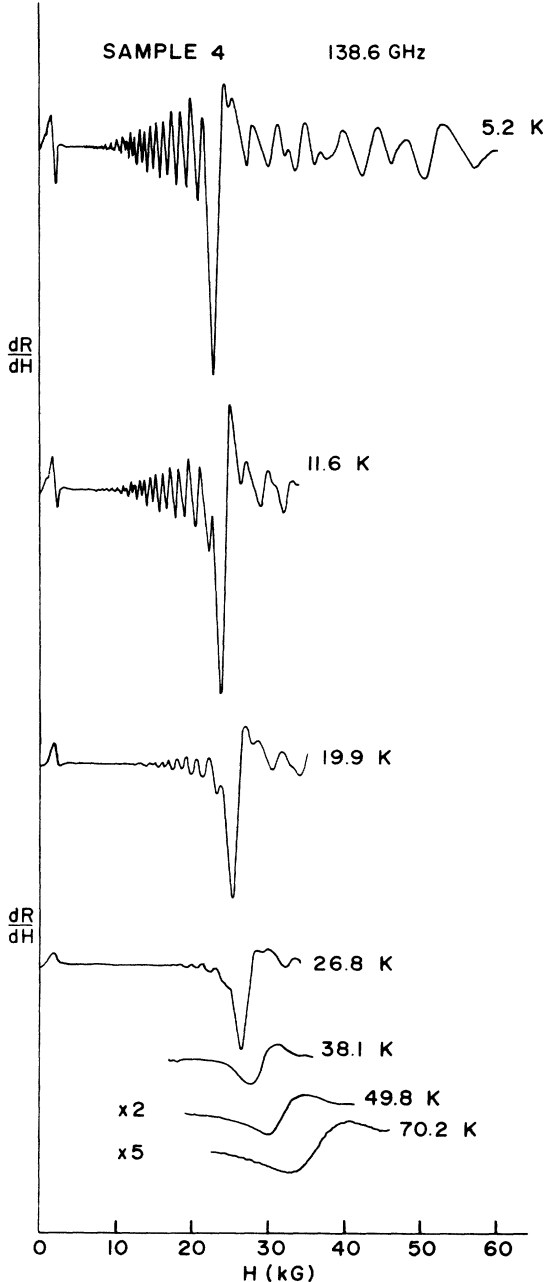


FIG. 12. Reflectivity data for sample 4 (bulk n -type) in the 2-mm band, showing the temperature dependence of the dielectric anomaly.

TABLE V. ω_{TO} and ϵ_s for n -type bulk samples computed from the self-consistent analysis.

Sample	ω_{TO} (4.2) (cm^{-1})	ϵ_s (4.2)	ϵ_∞ (4.2)	n (4.2) (cm^{-3})
4	12.0	2940	32.6	4.1×10^{17}
4	12.0	3238	35.9	4.52×10^{17}
4	12.0	3535	39.2	4.93×10^{17}
4 ^a	12.2	2850	32.6	3.25×10^{17}
4 ^a	12.2	3138	35.9	3.58×10^{17}
4 ^a	12.2	3427	39.2	3.91×10^{17}
6	12.5	2710	32.6	3.25×10^{17}
6	12.5	2984	35.9	3.58×10^{17}
6	12.5	3529	39.2	3.91×10^{17}

^aData taken approximately six weeks after first group tabulated.

$$f(H_a) = \frac{(\omega - \omega_3)(\omega^2 - \nu^2 - \omega_c^2) + 2\nu^2\omega}{(\omega^2 - \nu^2 - \omega_c^2)^2 + 4\nu^2\omega^2}. \quad (22)$$

We have neglected the phonon broadening parameter Γ , and it is understood that ω_3 and ω_c are to be evaluated at the field H_a at which the anomaly occurs. Thus $\epsilon_L(\omega)$ can be determined from the experimental frequency ω , the anomaly field H_a , the relaxation frequency ν (often negligible), the effective masses which enter ω_3 , ω_c , and ω_p , and the carrier concentration which enters ω_p . Given $\epsilon_L(\omega)$ and independent values of ϵ_∞ and ω_{LO} , ω_{TO} can be determined from Eq. (1). Now, as we shall see later, the reliability of our knowledge of ϵ_∞ and of the carrier concentration leaves something to be desired. It is therefore a considerable advantage to note that, for those samples with carrier concentration such that the anomaly can be observed in the available magnetic field range in both the 4- and 2-mm bands (all of our bulk samples except sample 1), ω_{TO} can be determined without independent knowledge of either ϵ_∞ or the carrier concentration. Suppose the anomaly is observed at fields H_{a1} and H_{a2} for experimental frequencies ω_1 and ω_2 . It then follows straightforwardly from Eqs. (21) and (22) that

$$\omega_{\text{TO}}^2 = (\alpha_1\beta_2\omega_2^2 - \alpha_2\beta_1\omega_1^2)/(\alpha_1\beta_2 - \alpha_2\beta_1), \quad (23)$$

where

$$\alpha_n = \omega_{\text{LO}}^2 - \omega_n^2, \quad \beta_n = f(H_{an})/\omega_n, \quad n = 1, 2.$$

Values of ω_{TO} determined self-consistently in this way are listed in the first column of Table V. We have used effective masses from the following paper¹⁶ and have assumed $\omega_{\text{LO}} = 114 \text{ cm}^{-1}$.³⁸ The computed average value of ω_{TO} at 4.2 K is 12.3 cm^{-1} with an estimated uncertainty of $\pm 1 \text{ cm}^{-1}$, mostly caused by uncertainties in determining the anomaly field in the absence of a detailed understanding of the anomaly signal line shape.

TABLE VI. Carrier concentrations for n -type bulk samples by phase-shift analysis. $T=4.2$ K.

Sample	Frequency (GHz)	ω_{TO} (cm^{-1})	n (cm^{-3})
4	68.6	12.0	2.7×10^{17}
4 ^a	72.4	12.2	2.0×10^{17}
6	65.7	12.5	1.7×10^{17}
7	66.0	12.2	1.3×10^{17}

^aData taken six weeks after first entry.

Consider now the determination of the carrier concentration. We have used three different methods: first, we have made Hall measurements, as discussed in Sec. III. Second, the carrier concentration can be calculated from the dielectric anomaly field, the ω_{TO} obtained self-consistently as described above, appropriate effective masses, and a value of ϵ_{∞} . Carrier concentrations obtained in this way for two samples are given in the last column of Table V. As discussed in detail below, there is some uncertainty about the value of ϵ_{∞} , so three different possible values are included in Table V. Whichever value is taken for ϵ_{∞} , it is apparent that the carrier concentrations obtained in this way are substantially larger than those obtained from the Hall measurements (Table III). Note, however, that the decrease with time of the carrier concentration in sample 4 is clearly apparent in data taken six weeks apart, just as in the Hall data. Note also that this change is accompanied by essentially no change in the value of the self-consistently determined value of ω_{TO} for this sample.

Finally, an independent determination of carrier concentration can be obtained from analysis of the helicon phase oscillations. We have fitted Eq. (11) to phase oscillation data for several samples. The results are shown in Table VI. The indicated values of ω_{TO} (obtained from self-consistent analyses) were used to calculate $\epsilon_L(\omega)$. (The fitted carrier concentration is relatively insensitive to the choice of ω_{TO} .) The phase oscillation data were obtained about three weeks before the Hall data shown in Fig. 7. Taking into account the time dependence of the carrier concentration, again clearly apparent in the Table VI entries for sample 4, the carrier concentrations derived from analysis of the helicon phase oscillations are seen to be in quite good agreement ($\sim 10\%$) with those obtained from Hall measurements.

We can, of course, derive values of ω_{TO} for our n -type samples using carrier concentrations obtained from Hall or helicon phase oscillation measurements. The results for two samples based on the phase oscillation carrier concentrations

and an assumed $\epsilon_{\infty}=32.6$ are given in Table VII. These ω_{TO} 's are 20% to 40% higher than the values obtained from the self-consistent analysis for these samples, because the phase oscillation carrier concentrations are lower than those inferred from the self-consistent analysis. Agreement between the two samples and for sample 4 at different times is no longer so good. Which set of ω_{TO} 's should be considered more reliable? In view of the uncertainties that we have discussed about carrier concentration drift and inhomogeneity, together with the questions implied by the latter about whether the various techniques really measure the same carrier concentration, we believe the values derived from the self-consistent analysis to be the more reliable.

The carrier concentration of our bulk p -type sample was sufficiently high to place the dielectric anomaly signal at 70 GHz above our maximum available magnetic field. Because we could observe the anomaly only at 140 GHz, we had no choice but to calculate ω_{TO} from the measured carrier concentration. Assuming $\epsilon_{\infty}=32.6$, the result (also listed in Table VII) was $\omega_{\text{TO}}=12.9 \pm 1.0$ cm^{-1} , in quite good agreement with the self-consistently derived values for the n -type samples.

We have mentioned that there is some uncertainty, at least in our minds, about the correct value of ϵ_{∞} to use in our calculations. Since ϵ_{∞} represents the contribution of electronic interband transitions to the polarizability, it can be expected to depend on temperature (because the electronic band structure does) and perhaps also on the carrier concentration. Previous workers appear, in general, to have favored the value $\epsilon_{\infty}=32.6$ quoted by Dixon and Riedl.²⁶ These authors, however, quote 32.6 as an average value over temperature and carrier concentration, while in making use of this value, other workers appear to have made no effort to correct it for the carrier concentration and temperature range appropriate to their own data. This may perhaps be justified on the grounds that Dixon and Riedl quote their value with an uncertainty of ± 2 , while their observed variation in ϵ_{∞} over the whole range of temperature (25–300

TABLE VII. ω_{TO} computed using measured carrier concentrations. $T=4.2$ K.

Sample	ω_{TO} (70 GHz) (cm^{-1})	ω_{TO} (140 GHz) (cm^{-1})
1	...	12.9 ± 1.0
4	16.2	15.8
4 ^a	15.4	15.0
6	17.8	17.4

^aData taken six weeks after second entry.

K) and carrier concentration ($3 \times 10^{18} - 5 \times 10^{19} \text{ cm}^{-3}$) is only slightly greater. Since we require ϵ_∞ in determining ω_{TO} from our data where the self-consistent scheme is inapplicable, and in using the Lyddane-Sachs-Teller relation to find the static dielectric constant $\epsilon_s = \epsilon_L(0)$ in any case, we consider it necessary to devote more attention to the matter of ϵ_∞ than appears to have been customary.

We are primarily concerned with the temperature dependence of ϵ_∞ through its dependence on the band gap E_g . Moss³⁹ has found that the empirical relationship $\epsilon_\infty^2 E_g = \text{constant}$ holds reasonably well for a number of semiconductors. Dionne and Woolley²⁷ have used another empirical relationship in their work on $\text{Pb}_{1-x}\text{Sn}_x\text{Te}$ alloys, namely:

$$\ln E_g = 1.65 - 0.086 \epsilon_\infty. \quad (24)$$

It is straightforward to show that such a relation is not unreasonable. Using the first Kramers-Kronig relation, ϵ_∞ may be shown to be of the form

$$\epsilon_\infty = A + B \ln E_g, \quad (25)$$

where A is a constant and $B = 2\epsilon_2(\omega)/\pi$. $\epsilon_2(\omega)$ is the imaginary part of the complex dielectric constant, and ω lies between the fundamental absorption edge $\omega_g = E_g/\hbar$ and some frequency ω_u above which $\epsilon_2(\omega)$ is essentially zero. In the range $\omega_g < \omega < \omega_u$, $\epsilon_2(\omega)$ is approximately constant; following Moss,³⁹ we here assume it has the value 16.5.

Lacking any solid basis for choosing among various possible values of ϵ_∞ , we have carried out our computations in the present work for three different values: (i) $\epsilon_\infty = 32.6$, independent of temperature. This is the Dixon and Riedl "average value." (ii) $\epsilon_\infty = 10.5[2.07 - \ln E_g(T)]$. A is here determined from the Zemel *et al.*⁴⁰ value of ϵ_∞ at 300 K, and E_g is in eV. (iii) $\epsilon_\infty = 10.5[1.76 - \ln E_g(T)]$. Here A is based on the Dixon and Riedl²⁶ value of ϵ_∞ at 84 K, and E_g is in eV. In each case, $E_g(T)$ is assumed to be given by¹ $E_g(T) = E_g(0) + \alpha T$, $E_g(0) = 0.187 \text{ eV}$ and $\alpha = 4.7 \times 10^{-4} \text{ eV/K}$. These three cases lead to values of $\epsilon_\infty(4.2)$ of 32.6, 39.2, and 35.9, respectively. It is these values which we have incorporated in Table V. Table V also gives values of the static lattice dielectric constant ϵ_s at $T = 4.2 \text{ K}$, calculated from $\omega_{\text{LO}} = 114 \text{ cm}^{-1}$ and the tabulated values of ω_{TO} and ϵ_∞ using the Lyddane-Sachs-Teller relation. The average values of ϵ_s computed over the three groups of experimental data are: $\epsilon_s(4.2) = 2830 \pm 450$ if $\epsilon_\infty(4.2) = 32.6$; $\epsilon_s(4.2) = 3120 \pm 500$ if $\epsilon_\infty(4.2) = 35.9$; $\epsilon_s(4.2) = 3410 \pm 550$ if $\epsilon_\infty(4.2) = 39.2$.

3. Temperature dependence of ω_{TO} - Curie temperature

In the field and frequency range where the dielectric anomaly of principal interest here is observed, $\omega_c \gg \omega$ and the condition for the anomaly is approximately $\epsilon_L = \omega_p^2/\omega\omega_c$. Furthermore, $\omega < \omega_{\text{TO}}$, so that $\epsilon_L \cong \epsilon_s$. It follows that if ϵ_s has a Curie-law paraelectric temperature dependence, $\epsilon_s \propto (T - T_C)^{-1}$, we expect the anomaly field to vary with temperature approximately linearly as $T - T_C$. Figure 12 shows that the anomaly field does indeed increase with increasing temperature and linearly at higher temperatures.

We have analyzed our data on the temperature dependence of the anomaly field to determine the Curie temperature T_C . The analysis was made only for those bulk samples which satisfied the criterion of reproducibility set forth previously. The data for other samples, which in many cases displayed well-defined anomalies with the expected temperature dependence, were rejected. We did this because we felt that T_C 's obtained from samples for which there were indications of less than maximum crystalline perfection were of doubtful value, since T_C may be expected to be rather sensitive to the state of the lattice. ω_{TO} was determined from the anomaly condition $\text{Re}\epsilon = 0$ for each sample at each temperature, assuming the following:

- A temperature-independent carrier concentration derived from the self-consistent two-frequency analysis of the low-temperature data.
- A temperature-dependent cyclotron mass derived from the band model described in the following paper,¹⁶ assuming that the energy gap depends linearly on temperature as given in the previous section.
- A temperature-independent mass anisotropy ratio. The values $K_c = 10$, $K_v = 13$ were used throughout the analysis. While neither these values nor the assumption that they are temperature independent precisely represents the situation for lead telluride (as the analysis in the following paper¹⁶ indicates), the error in T_C caused by the use of these assumptions is insignificant compared with the experimental uncertainties from other sources. We estimate the total uncertainty at about 5%.
- An electron damping constant ν having a temperature dependence consistent with the experimentally measured anomaly linewidths, and a temperature-independent phonon damping constant $\Gamma = 3.5 \text{ cm}^{-1}$. This is based on our observation (see Sec. V A 5) that the anomaly linewidths appear to be determined primarily by electronic damping and are relatively insensitive to the value of Γ .
- The several different possible choices for

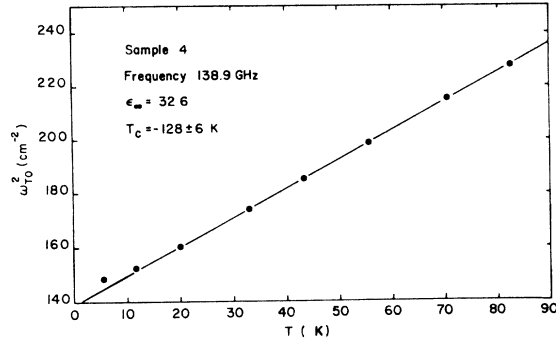


FIG. 13. ω_{T0}^2 vs temperature for sample 1 (bulk p -type), assuming $\epsilon_\infty = 32.6$.

ϵ_∞ and its temperature dependence discussed in Sec. VA 2.

The exception to the use of this procedure was sample 1, for which no effective masses or carrier concentration from our own self-consistent analysis were available. For this sample, the carrier concentration determined from thermoelectric data and quoted in Table IV was assumed. The transverse mass at the Fermi energy was calculated from the multiband model¹⁶ using a valence-band-edge mass of $0.021 m_0$ and a band edge mass anisotropy ratio of 13.

A plot of ω_{T0}^2 determined by this method is plotted versus temperature for $\epsilon_\infty = 32.6$ in Fig. 13 for sample 4. It is similar to the Bate *et al.*¹⁴ (capacitance)^{-3/2} vs T plot. The plot is linear for temperatures above 20 K. Below this temperature, ω_{T0}^2 decreases less rapidly than linearly and appears to become temperature independent as $T \rightarrow 0$. Bate *et al.* offered no explanation for their observation of this feature and neither can we. A linear least-squares fit to the data for $T > 30$ K is shown in Fig. 13. It yields a $T_C = -128 \pm 6$ K. A similar

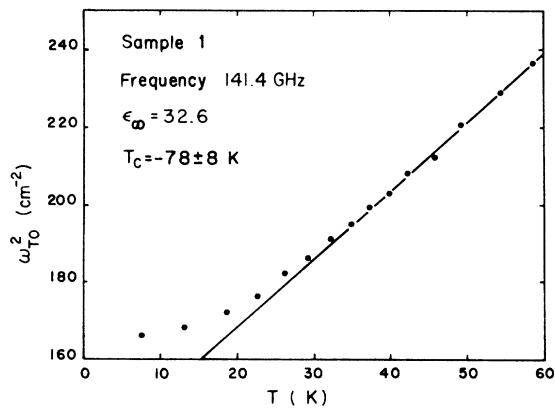


FIG. 14. ω_{T0}^2 vs temperature for sample 1 (bulk p -type), assuming $\epsilon_\infty = 32.6$.

TABLE VIII. Curie temperatures.

Sample	ϵ_∞ (4.2 K)	T_C (K)	ω_{T0} (295 K) ^a
1	32.6	-78 ± 8	27.4 ± 0.9
	35.9	-87 ± 9	26.4 ± 1.0
	39.2	-85 ± 9	26.6 ± 0.9
4	32.6	-129 ± 6	21.4 ± 2.1
	35.9	-153 ± 7	20.3 ± 2.0
	39.2	-151 ± 7	20.3 ± 2.0
4 ^b	32.6	-127 ± 6	21.9 ± 2.1
	35.9	-151 ± 7	20.7 ± 2.0
	39.2	-148 ± 7	20.8 ± 2.0
6	32.6	-128 ± 6	22.4 ± 2.1
	35.9	-150 ± 7	21.2 ± 2.0
	39.2	-148 ± 7	21.3 ± 2.0
Direct room- temperature measurement (Ref. 13)	32.6		$22.9^{+4.0}_{-2.6}$
	35.9		$22.0^{+3.8}_{-2.5}$
	39.2		$23.2^{+4.1}_{-2.6}$

^aValues in sets 1, 4, 4,^b and 6 obtained by Curie-law extrapolation from low temperatures.

^bData taken six weeks after that for previous entry.

Curie-law plot for sample 1 is shown in Fig. 14.

Values of T_C derived from analyses of this sort using the several assumptions about ϵ_∞ and its temperature dependence are assembled in Table VIII. Also included are values of ω_{T0} extrapolated to room temperature assuming that the Curie-law dependence of ϵ_s holds between our maximum experimental temperature (~ 80 K) and room temperature. For comparison we list values derived from a room-temperature determination of ϵ_s by the authors¹³ using a microwave cavity perturbation technique. The values of ω_{T0} depend somewhat on the $\epsilon_\infty(T)$ used. The agreement between our results for samples 4 and 6, both n -type samples prepared in our laboratory, is excellent. The T_C 's for these two samples compare favorably with the value $T_C = -135$ K inferred from neutron-inelastic-scattering data by Alperin *et al.*⁸ However, the T_C for sample 1, a p -type sample, is significantly (algebraically) higher, and is in rather close agreement with the value $T_C = -78$ K obtained from p - n junction capacitance measurements by Bate *et al.*¹⁴ While it is possible that the difference represents an intrinsic effect, perhaps a dependence of T_C on carrier type and concentration, we are inclined to believe that the lower T_C 's obtained for the n -type samples more closely approximate the T_C of pure unstrained and otherwise unperturbed bulk PbTe. Our reasons for this belief include the following: (i) Our other n -type samples, rejected because

they failed to satisfy our criterion of reproducibility, tended to yield significantly higher T_C 's than samples 4 and 6. (ii) The extrapolations to room temperature using the lower T_C 's agree rather better with our room-temperature experimental results¹³ than those for the higher T_C 's. In this connection, it should be noted that the p - n junction capacitance measurements of Bate *et al.*, which were done over the full temperature range between helium temperatures and room temperature, indicate that the Curie-law temperature dependence is followed over the full range. (iii) It seems possible that the T_C obtained by Bate *et al.* may be too high because of built-in electric field effects in their p - n junctions, even though their junctions were much wider than those in the early experiments of Kanai and Shohno,² where such effects appear to have led to the deduction of much too small a lattice dielectric constant. The bulk-crystal neutron experiments of Alperin *et al.*⁶ should be free of such problems.

4. Effective masses

We have determined cyclotron effective masses from the cyclotron resonance signals observed in the course of these experiments. Several factors must be taken into account in interpreting these signals. The first is the fact that the resonance is accompanied by a nearby dielectric anomaly (see Fig. 2). The observed line thus represents a broadened superposition of a resonance and a dielectric anomaly, and this complicates the determination of the resonance field. We have not attempted any detailed line-shape fitting, but have sidestepped the issue by assigning an experimental uncertainty which includes (and is dominated by) the uncertainty in assignment of the resonance field.

The second factor is the fact that our bulk-sample data all correspond to a single magnetic field orientation, $\vec{H} \parallel \langle 100 \rangle$. In this orientation a single cyclotron resonance signal is observed, corresponding to a cyclotron effective mass which depends on *two* parameters of the near-spheroidal PbTe Fermi surface—the transverse effective mass and either the longitudinal effective mass or their ratio, the mass anisotropy ratio. The two cannot be independently determined from our data. The procedure we followed, therefore, was to *assume* a value of 10 for the conduction-band mass anisotropy ratio and to interpret our resonance data in terms of the transverse effective mass. The analysis of the following paper¹⁶ indicates that this value of the mass anisotropy ratio is too high, but the effect on our results of correcting it is negligible compared with our experi-

mental uncertainty.

The transverse effective masses obtained in this way must be corrected for nonlocal effects. We have done this using the formalism discussed in Sec. IID. The resulting (downward) nonlocal corrections ranged from 16% in the lowest concentration sample to 28% in the highest concentration sample.

Finally, it is most useful to not report the measured (corrected) transverse effective mass at the Fermi surface, but the band-edge transverse effective mass. This requires a small (and again downward) correction for band nonparabolicity. This was done using the multiband model discussed in the following paper.¹⁶ The final band-edge masses for all six of our n -type samples are listed in Table IX. We were able to use data from all of these samples because the cyclotron resonance signals were observed to be uninfluenced by the sample condition problems which plagued the dielectric anomaly measurements. The agreement among the samples is rather good. The average conduction-band-edge transverse effective mass is $m_{1c}/m_0 = 0.0164 \pm 0.0010$. This is significantly smaller than all previously reported values. The implications of this fact are discussed in detail in the following paper.¹⁶ It should be noted that no adequate cyclotron resonance data were available to enable a mass determination for sample 1.

5. Damping constants

The theory we have used to analyze our experiments contains two phenomenological damping constants, ν for the free carriers and Γ for the lattice. It is of interest to see what may be concluded about these two parameters from the observed widths of the cyclotron resonance and dielectric anomaly signals.

We expect the cyclotron resonance linewidth to be determined largely by ν . We have made calculations of the line shape and width which should be expected for the cyclotron resonance and adjacent dielectric anomaly assuming a semi-infinite sam-

TABLE IX. Band-edge effective masses for n -type bulk samples.

Sample	Frequency (GHz)	$\rho^{1/3}$	m_{1c}/m_0
2	141.4	0.206	0.0162
3	138.2	0.284	0.0165
4	141.4	0.267	0.0155
5	141.4	0.161	0.0177
6	141.4	0.242	0.0165
7	139.95	0.194	0.0162

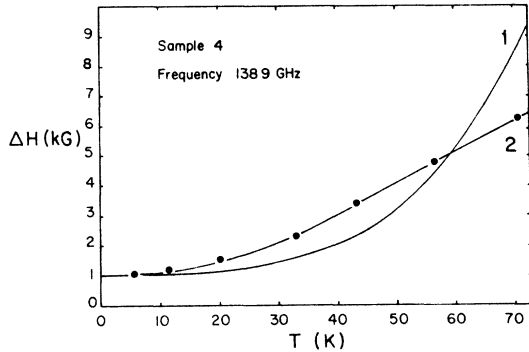


FIG. 15. Calculated (1) and observed (2) dielectric anomaly linewidths vs temperature.

ple, so that only the first-surface reflectivity is taken into account. When free-carrier damping constants (inverse relaxation times) deduced from the measured Hall mobility are inserted in the results, we find good agreement with the widths and reasonable agreement with the shapes of the experimentally observed resonance lines. This comparison can, of course, be made only at the lowest temperatures, because ν increases rapidly with temperature and the cyclotron resonance line broadens and becomes unobservable above about 30 K. Over this range of temperatures, however, the damping constants deduced from the Hall mobility appear to account quantitatively for the observed cyclotron resonance linewidths.

The linewidth of the high-field dielectric anomaly may depend on both ν and Γ , since it arises from a cancellation of the free-carrier and lattice dielectric constants in a region where the influence of damping on the free-carrier dielectric constant is relatively small. We have calculated the shape and width of the dielectric anomaly signal for a semi-infinite sample. Curve 1 in Fig. 15 shows the peak-to-valley width of the dielectric anomaly signal calculated using the free-carrier damping constants deduced from our Hall mobility measurements and assuming that the lattice damping constant Γ is negligible. The agreement with the experimental widths (curve 2) at low temperatures indicates that the contribution of Γ there is small compared with that of ν , and allows us to place a rough upper limit on it. For our best bulk samples we find $\Gamma(4.2 \text{ K}) \leq 3.5 \text{ cm}^{-1}$. In other bulk samples, there is some indication that Γ may be higher.

As the temperature increases, the anomaly linewidth becomes somewhat larger than expected from the increasing free-carrier damping alone. This might be interpreted as evidence for an increasing Γ . However, at the highest temperatures, the linewidth is less than expected from free-

carrier damping alone! This disagreement is perhaps not surprising. The model dielectric function we have used assumes independent oscillators for the lattice and the free-carrier plasma. This is probably a reasonable assumption in the limit of small damping, i.e., at 4.2 K. However, as Kukharskii⁴¹ has shown, it is doubtful whether it is appropriate in the higher-temperature regime. Here a model in which the parameters, both eigenfrequencies and damping constants, are those of the coupled phonon-plasmon system, is more likely to be appropriate. We have not investigated this question. Our interest in the temperature dependence of the damping constants in these experiments relates only to possible corrections in estimating Curie temperatures. The magnitude of $\nu(T)$ estimated from the anomaly linewidths is sufficiently small that it implies negligible corrections in the Curie-temperature calculations, and the precise form of $\nu(T)$ is therefore not crucial.

B. Thin-film results

Our experimental results for the *p*-type epitaxial thin-film samples are for a variety of reasons more complex and less informative in the present context than our bulk-sample results. First, their crystal orientation required $\vec{H} \parallel \langle 111 \rangle$ and this leads to a more complex pattern of cyclotron resonances and dielectric anomalies than for the $\vec{H} \parallel \langle 100 \rangle$ bulk-sample orientation (see Fig. 3). Second, they were sufficiently thin that back-surface reflection effects could be important at all fields. Finally, there is the recent evidence of Houston *et al.*⁴² that in *n*-PbTe epitaxial films on BaF₂ substrates, strain owing to differential thermal contraction on cooling to helium temperatures can cause a substantial splitting of the normally degenerate band edges and a transfer of all the carriers into the single ellipsoid with long axis normal to the film plane. In view of these complications, we have not based any of our final conclusions strongly on the thin-film data. However, the data are interesting, and we therefore describe them briefly here as a motivation and aid for further investigation. Our tentative identification of some of the observed features is based on the model dielectric function used elsewhere in this paper. If all the carriers were indeed in a single ellipsoid as suggested by the results of Houston *et al.*, the free-carrier contribution to the dielectric constant would be modified and our interpretation subject to change.

Figure 16 is a plot of dielectric anomaly loci for the field orientation, carrier concentrations, and masses appropriate to our thin-film samples. It is evident that for $\omega_{TO} = 12 \text{ cm}^{-1}$, the ω_0^- anomaly appears only at 70 GHz, and then at relatively low

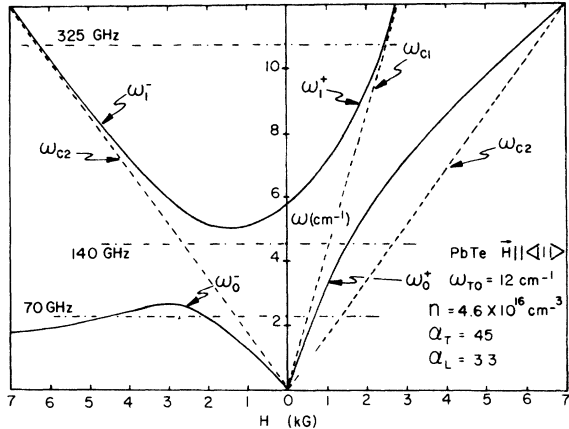


FIG. 16. Dielectric anomaly loci for $\vec{H} \parallel (111)$ and parameters appropriate to the p -type thin-film samples.

fields (≈ 5 kG). Data for sample 8 at 70 GHz as a function of temperature are illustrated in Fig. 17. We associate the large dip at about 5 kG with the ω_0^- anomaly. Substantial motion of this minimum to higher fields with increasing temperature is observed, while the other principal features of the spectrum remain substantially stationary. Other data for this sample confirm the motion of the ω_0^- anomaly to lower fields with increasing frequency, again in agreement with expected behavior. The anomaly is much broader than for the bulk samples, and the assignment of the anomaly field H_a correspondingly less precise. However, calculation indicates that $\partial H_a / \partial \omega_{TO} > 1$ kG/cm $^{-1}$ in this region. The estimated uncertainty in the determination of ω_{TO} is, therefore, conservatively estimated as ± 1.5 cm $^{-1}$. The remaining structure is associated with the two cyclotron resonances and low-field ω_0^+ and ω_0^- anomalies. Clearly, the cyclotron

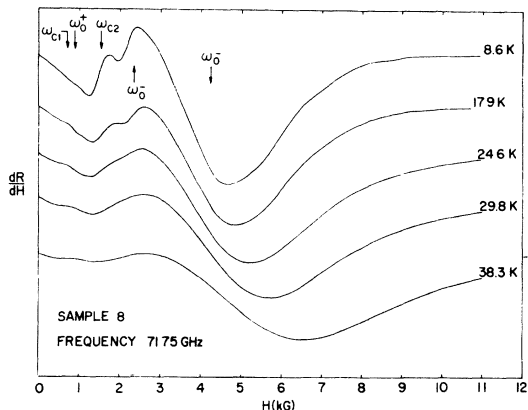


FIG. 17. Reflectivity data for sample 8 (thin-film p -type) in the 4-mm band with $\vec{H} \parallel (111)$.

resonances at 70 GHz are too poorly defined to permit measurement of the effective masses.

Typical experimental traces at 140 GHz for sample 9 are shown in Fig. 18 for two temperatures. The data at this frequency are much less informative with respect to the location of ω_{TO} . For $11 < \omega_{TO} < 22$ cm $^{-1}$, ω is expected to lie between the maximum in ω_0^- and the minimum in ω_1^- . Since we appear to see no temperature-dependent structure associated with either of these anomalies, we can only conclude that ω_{TO} probably lies somewhere between 11 and 22 cm $^{-1}$.

The approximate locations of several expected features are designated on the figure. There are some puzzles connected with the interpretation of the observed structures. First, what by its location should be the ω_{c1} cyclotron resonance has a curiously enhanced amplitude for temperatures somewhat greater than 10 K. This behavior has been observed at both 140 and 335 GHz. Second, for any reasonable ω_{TO} no structure is expected above ω_{c2} . However, we observe two rather well-defined dips at fields near 4.5 and 8.5 kG which broaden with increasing temperature much as a cyclotron resonance would. Within the rather limited range of frequencies available, the fields at which the dips occur appear to be proportional to frequency, as for a cyclotron resonance. Furthermore, these dips occur suggestively close to three times the fields at which the dips which might be ω_{c1} and ω_{c2} occur. (This is not, however, what one would expect if there were large strain-induced trigonal warpings of the Fermi spheroids. Such warping would produce subharmonic signals at $\frac{1}{3}$, not three times the fundamental resonance fields.)

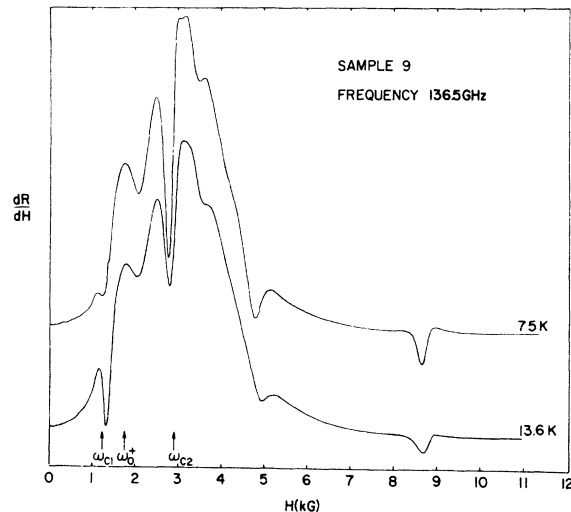


FIG. 18. Reflectivity data for sample 9 (thin-film p -type) in the 2-mm band with $\vec{H} \parallel (111)$.

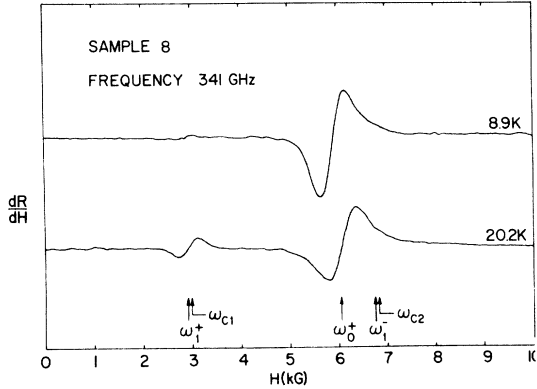


FIG. 19. Reflectivity data for sample 8 (thin-film p -type) at 341 GHz with $\vec{H} \parallel \langle 111 \rangle$.

None of these characteristics lend support to an interpretation that these high-fields dips are perhaps dielectric anomalies produced by an ω_{TO} strongly shifted by, say, surface band-bending effects. An explanation based on the strain-redistributed-carrier picture of Houston *et al.*⁴² should be explored, but we have not done so. We note only that if the large and sharp dip near the field expected for ω_{c2} is in fact the high-mass cyclotron resonance, all of the carriers *cannot* be in a single ellipsoid as suggested by Houston *et al.*

The data taken at 341 GHz for sample 8 are shown in Fig. 19 for two temperatures. The expected positions of resonances and anomalies are again indicated. The spectrum at this frequency is relatively simple. The lower resonance is probably ω_{c1} , together with the ω_1^+ anomaly which should lie rather close to it. The structure at higher fields is probably a superposition of the ω_{c2} resonance and the ω_0^+ and ω_1^- anomalies. The same anomalous temperature dependence of the amplitude of the suspected ω_{c1} resonance observed in the 140 GHz band is again present. In Fig. 20, data for the same sample at 321 GHz show the appearance of additional structure in the high-field signal. We interpret this as a result of shifting of the ω_0^+ anomaly to lower fields with decreasing frequency, exposing the ω_{c2} resonance and ω_1^- anomaly. The anomalous temperature dependence of the structure at lower fields is once again apparent.

The anomaly loci plots, in conjunction with line-shape calculations, suggest an ω_{TO} somewhere between 12 and 15 cm^{-1} , in reasonable agreement with the conclusions drawn from the 70-GHz data. All the evidence from the 335-GHz band indicates that ω_{TO} certainly lies above the highest frequency (≈ 345 GHz) experimentally available. Our inferences about ω_{TO} from the thin-film samples are

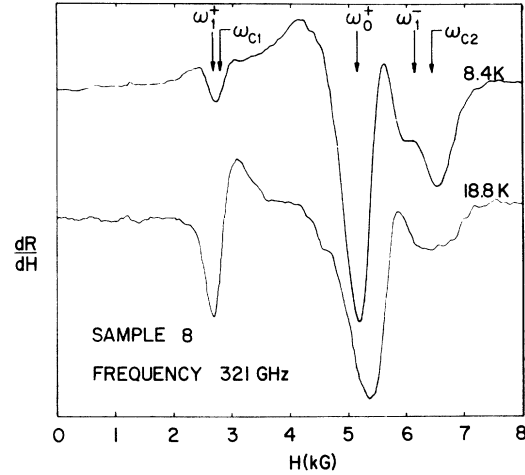


FIG. 20. Reflectivity data for sample 8 (thin-film p -type) at 321 GHz with $\vec{H} \parallel \langle 111 \rangle$.

listed in Table X. The results are seen to be generally consistent with values obtained from bulk sample measurements.

We have deduced effective masses from the thin-film results, assuming that the dips observed near the expected positions of the ω_{c1} and ω_{c2} cyclotron resonances are in fact those resonances. Since two resonances are observed for $\vec{H} \parallel \langle 111 \rangle$, the transverse effective mass and the mass anisotropy ratio can be independently determined. Because of the very small carrier concentrations of the thin-film samples and the high experimental frequencies, the nonlocal and nonparabolicity corrections are almost negligible. The results are collected in Table XI. The resulting average valence-band-edge parameters are $m_w/m_0 = 0.021 \pm 0.001$, $K_{ov} = 13.4 \pm 2$. These are in excellent agreement with other measurements,¹⁶ a fact which gives us some confidence that our identification of the ω_{c1} and ω_{c2} resonances is indeed correct. It also suggests that complete transfer of carriers to a single valley never occurs for our p -type samples in contrast to the results of Houston *et al.*⁴² for n -type films. It seems possible however, that the curious temperature dependence of the amplitude of the low-field cyclotron resonance may be explained on the basis of some strain-induced splitting of the valleys accompanied

TABLE X. ω_{TO} for p -type thin-film samples.

Sample	$\omega_{TO}(70 \text{ GHz})$ (cm^{-1})	$\omega_{TO}(140 \text{ GHz})$ (cm^{-1})	$\omega_{TO}(340 \text{ GHz})$ (cm^{-1})
8	12 ± 1.5	11–22	12–15
9	12 ± 1.5	11–22	12–15

TABLE XI. Band-edge effective masses for *p*-type thin-film samples.

Sample	Frequency (GHz)	$\rho_1^{1/3}$	$\rho_2^{1/3}$	m_{1v}/m_0	m_{3v}/m_0	K_{0v}
8	342	0.030	0.069	0.0212
8	321	0.032	0.072	0.0207	0.313	15.1
8	333	0.031	0.070	0.0207	0.303	14.6
9	328	0.031	0.071	0.0214	0.266	12.4
9	137.75	0.056	0.127	0.0209	0.245	11.7

by a corresponding transfer of carriers.

Very recently several reports on magneto-optical measurements on *n*-type epitaxial thin films of PbTe by Burkhard *et al.*⁴³⁻⁴⁶ came to our attention. These authors report direct observation of the TO phonon frequency at $T = 5, 77,$ and 300 K, yielding values of $\omega_{TO} = 18, 23,$ and 32 cm^{-1} , respectively. This work provides another confirmation of the strong temperature dependence of ω_{TO} in PbTe. The low-temperature value is in agreement with the result of Buss and Kinch¹⁰ but not with our present value. No carrier transfer between valleys caused by strain effects of the type reported by Houston *et al.*⁴² were observed. Multiparameter fits to the magnetorefectivity yielded transverse-conduction-band-edge masses significantly larger than the value we report here. It is difficult to assess the disagreements between our results and those of Burkhard *et al.* because the latter result from fitting models to data using parameters which in some cases are not well established for PbTe, and because the sensitivity of the fits to parameter variation are not discussed. Moreover, as the data and discussion of the present paper indicate, results obtained from epitaxial thin films are not necessarily representative of the bulk material.

V. SUMMARY AND CONCLUSIONS

The principal objectives of this work were a determination of the transverse optic phonon frequency and the static lattice dielectric constant of PbTe and a resolution of the long standing large discrepancies among experimentally determined values of these parameters. On the basis of the results and discussion of Sec. IV, we draw the following principal conclusions.

(a) The best experimental value of the $q=0$ transverse-optic phonon frequency at low temperatures is $\omega_{TO(4.2)} = 12.3 \pm 1.0$ cm^{-1} . This is consistent with our results for both *n*- and *p*-type bulk samples and *p*-type epitaxial thin-film samples.

(b) This ω_{TO} implies, through the Lyddane-Sachs-Teller relation, a low-temperature static lattice dielectric constant of about 3000. The uncertainty in this number is dominated by uncer-

tainty about the low-temperature value of the high-frequency dielectric constant, ϵ_∞ .

(c) We confirm that PbTe is indeed paraelectric, with the static lattice dielectric constant displaying a Curie-law temperature dependence $\epsilon_s \propto (T - T_C)^{-1}$ above about 30 K. ω_{TO} shows a corresponding temperature dependence, $\omega_{TO} \propto (T - T_C)^{1/2}$. This Curie-law dependence is found in the present experiments up to about 80 K. Comparison of values of ϵ_s extrapolated to room temperature with a value experimentally determined at room temperature using a microwave cavity perturbation technique¹³ indicates that the Curie-law behavior extends at least over the temperature range $30 \lesssim T < 300$ K. We find values of T_C grouped near both -150 and -80 K, but for a variety of reasons we favor the value $T_C = -151 \pm 7$ K as the best representation of the Curie temperature of PbTe.

(d) We find the following band-edge electronic parameters: transverse-conduction-band-edge effective mass, $m_{1c}/m_0 = 0.0164 \pm 0.001$; transverse-valence-band-edge effective mass, $m_{1v}/m_0 = 0.021 \pm 0.001$; valence-band-edge mass anisotropy ratio, $K_{0v} = 13.4 \pm 2.0$. These valence-band parameters agree well with previous measurements. Our conduction-band-edge effective mass is significantly smaller than previously measured values.

The wide range of reported values of the static lattice dielectric constant of PbTe is, of course, due in part to its strong temperature dependence, first observed by Bate *et al.*¹⁴ and confirmed here. We believe that it is also due in part to the extreme sensitivity of PbTe to sample fabrication procedures. On the basis of our own experience, we feel that any experimental value of the static lattice dielectric constant which has not been demonstrated to be unaffected by improvements in sample preparation methods must be considered suspect. Although we cannot prove that we have done everything necessary to assure that we have determined the true static lattice dielectric constant of PbTe, we are inclined to view our result like a variational calculation of an upper bound on a ground-state energy: Since all of the factors we can think of which might influence ω_{TO} and ϵ_s (e.g.,

strain, electric fields due to surface band bending) would tend to increase ω_{TO} and decrease ϵ_s , the fact that our ω_{TO} is smaller and our ϵ_s is larger than most previously reported values suggests that our results are at least closer to the truth than these earlier values.

ACKNOWLEDGMENTS

We would like to thank Dr. A. J. Strauss and Dr. H. Holloway for their generous donation of samples and Dr. A. Denenstein for many helpful discussions on experimental technique.

- †Research supported by the NSF under Grant No. GP-40376 and by the Advanced Research Projects Agency of the Dept. of Defense as monitored by the Air Force Office of Scientific Research under Contract No. F44620-75-C-0069.
- *Present address: Dept. of Electrical Engineering and Science, Moore School, University of Pennsylvania, Philadelphia, Pa. 19104.
- ¹R. Dalven, in *Solid State Physics*, edited by H. Ehrenreich, F. Seitz, and D. Turnbull (Academic, New York, 1973), Vol. 28, p. 179.
 - ²Y. Kanai and K. Shohno, *Jpn. J. Appl. Phys.* **2**, 6 (1963).
 - ³H. M. Day and A. C. MacPherson, *Proc. IEEE* **51**, 1362 (1963).
 - ⁴N. Watanabe, *Jpn. J. Appl. Phys.* **3**, 166 (1964).
 - ⁵W. Cochran, R. A. Cowley, G. Dolling, and M. M. Elcombe, *Proc. R. Soc. Lond. A* **293**, 433 (1966).
 - ⁶H. A. Alperin, S. J. Pickart, and J. J. Rhyne, *Phys. Lett. A* **40**, 4 (1972).
 - ⁷E. G. Bylander and M. Hass, *Solid State Commun.* **4**, 51 (1961).
 - ⁸Y. Sawada, E. Burstein, D. L. Carter, and L. Testardi, in *Plasma Effects in Solids*, edited by J. Bok (Dunod, Paris, 1964), p. 71.
 - ⁹S. Perkowitz, *Phys. Rev.* **182**, 828 (1969).
 - ¹⁰D. D. Buss and M. A. Kinch, in *Proceedings of the Conference on the Physics of IV-VI Compounds and Alloys*, edited by S. Rabii (Gordon and Breach, London, 1974), p. 209.
 - ¹¹J. Mygind, thesis (Technical University of Denmark, 1972) (unpublished).
 - ¹²S. Takano, S. Hotta, H. Kawamura, Y. Kato, K. L. I. Kobayashi, and K. F. Komatsubara, *J. Phys. Soc. Jpn.* **37**, 1007 (1974).
 - ¹³G. M. T. Foley and D. N. Langenberg, *Solid State Commun.* **18**, 351 (1976).
 - ¹⁴R. T. Bate, D. L. Carter, and J. S. Wrobel, *Phys. Rev. Lett.* **25**, 159 (1970).
 - ¹⁵G. M. T. Foley and D. N. Langenberg, *Bull. Am. Phys. Soc.* **19**, 235 (1974).
 - ¹⁶G. M. T. Foley and D. N. Langenberg, following paper, *Phys. Rev. B* **15**, 4850 (1977).
 - ¹⁷B. B. Varga, *Phys. Rev.* **137**, A1896 (1965).
 - ¹⁸M. Born and K. Huang, *Dynamical Theory of Crystal Lattices* (Oxford U. P., London, 1954).
 - ¹⁹R. H. Lyddane, R. G. Sachs, and E. Teller, *Phys. Rev.* **59**, 673 (1941).
 - ²⁰P. R. Wallace, *Can. J. Phys.* **43**, 2162 (1965).
 - ²¹P. B. Miller and R. R. Haering, *Phys. Rev.* **128**, 126 (1962).
 - ²²S. Perkowitz, Ph.D. thesis (University of Pennsylvania, 1966) (unpublished).
 - ²³R. F. Brebrick and E. Gubner, *J. Chem. Phys.* **36**, 1283 (1962).
 - ²⁴D. G. Coates, W. D. Lawson, and A. C. Prior, *J. Electrochem. Soc.* **108**, 1038 (1961).
 - ²⁵I. Bucklow and M. Cole, *Metallurgical Rev.* **135**, 103 (1969).
 - ²⁶J. R. Dixon and H. R. Riedl, *Phys. Rev.* **138**, A873 (1963).
 - ²⁷G. Dionne and J. C. Woolley, *Phys. Rev. B* **6**, 3898 (1972).
 - ²⁸K. Norr, NOLTR 63-156, U. S. Naval Research Lab. Report, Maryland, 1963 (unpublished).
 - ²⁹G. Dionne and J. C. Woolley, *J. Electrochem. Soc.* **119**, 784 (1972).
 - ³⁰N. J. Parada and G. W. Pratt, Jr., *Phys. Rev. Lett.* **22**, 180 (1969).
 - ³¹A. J. Strauss, *J. Electronic Mater.* **2**, 553 (1973).
 - ³²R. S. Allgaier and B. B. Houston, in *Proceedings of the International Conference on the Physics of Semiconductors*, edited by A. C. Strickland (Institute of Physics and The Physical Society, London, 1962), p. 172.
 - ³³J. N. Walpole, thesis (MIT, 1966) (unpublished).
 - ³⁴A. J. Strauss, in *Proceedings of the Conference on the Physics of IV-VI Compounds and Alloys*, edited by S. Rabii (Gordon and Breach, London, 1974), p. 227.
 - ³⁵J. N. Walpole and A. L. McWhorter, *Phys. Rev.* **158**, 708 (1967).
 - ³⁶A. J. Strauss (private communication).
 - ³⁷K. Shogenji and S. Uchiyama, *J. Phys. Soc. Jpn.* **12**, 252 (1957).
 - ³⁸R. N. Hall and J. N. Racette, *J. Appl. Phys. Suppl.* **32**, 2078 (1961).
 - ³⁹T. Moss, *Optical Properties of Semiconductors; A Semiconductor Monograph* (Butterworths, London, 1959).
 - ⁴⁰J. N. Zemel, J. D. Jensen, and R. B. Schoolar, *Phys. Rev.* **140**, A330 (1965).
 - ⁴¹A. A. Kukharskii, *Solid State Commun.* **13**, 1761 (1973).
 - ⁴²B. B. Houston, J. R. Burke, and G. P. Carver, *Bull. Am. Phys. Soc.* **21**, 378 (1976).
 - ⁴³H. Burkhard, G. Bauer, and A. Lopez-Otero, *Solid State Commun.* **18**, 773 (1976).
 - ⁴⁴H. Burkhard, G. Bauer, P. Grosse, and A. Lopez-Otero, *Phys. Status Solidi* **76**, 259 (1976).
 - ⁴⁵H. Burkhard, G. Bauer, P. Grosse, and A. Lopez-Otero, in *Proceedings of the Thirteenth International Conference on the Physics of Semiconductors*, Rome, 1976 (unpublished).
 - ⁴⁶H. Burkhard, G. Bauer, P. Grosse, and A. Lopez-Otero, in *Proceedings of the International Conference on Magneto-optics*, Zürich, 1976 (unpublished).